Available online at www.sciencedirect.com
ScienceDirect
Journal of Nuclear Materials 361 (2007) 218–227
journal of nuclear materials
www.elsevier.com/locate/jnucmat

Deformation microstructure of proton-irradiated stainless steels

Z. Jiao [a,*], J.T. Busby [b], G.S. Was [a]

[a] Department of Nuclear Engineering and Radiological Sciences, University of Michigan, Ann Arbor, MI 48109, United States
[b] Materials Science and Technology Division, Oak Ridge National Laboratory, Oak Ridge, TN 37831, United States

Abstract

The deformation microstructure of proton-irradiated stainless steels may play a key role in explaining their irradiation-assisted stress corrosion cracking (IASCC) susceptibility. In the present study, three model alloys (UHP-304, 304 + Si, 304 + Cr + Ni) with different stacking fault energies (SFEs) were irradiated with 3.2 MeV protons at 360 °C to 1.0 and 5.5 dpa and then strained in 288 °C Ar atmosphere. The deformation microstructure of the strained samples was investigated using scanning electron microscopy and transmission electron microscopy. The results showed that the slip lines interacted with grain boundaries by grain-to-grain transmission, grain boundary sliding or deformation ledge formation at grain boundaries. Expanded channels, which were formed at locations where dislocation channels intersected the grain boundaries or other channels, were found predominately in the low SFE alloys UHP-304 and 304 + Si. The steps and shear strain at grain boundaries caused by channel expansion may increase the IASCC susceptibility in low SFE stainless steels by producing strain concentrations and inducing cracks in the oxide film.
© 2006 Elsevier B.V. All rights reserved.

1. Introduction

Irradiation assisted stress corrosion cracking (IASCC) has been a problem in the nuclear industry for the last 30 years. It is most important in core component cracking in boiling water reactors (BWR) and is of growing importance in pressurized water reactors (PWR). An understanding of the mechanism of IASCC is required in order to provide guidance for the development of mitigation strategies. IASCC is affected by changes to both the water environment and the microstructure of the irradiated alloy [1]. However, the changes to the microstructure are the real concern since IASCC can be replicated in the laboratory by conducting post-irradiation stress corrosion cracking tests. In essence, changes to the environment can alter the severity of the cracking, but it is the irradiation-induced change to the microstructure that triggers the occurrence of IASCC.

One of the principal reasons why the IASCC mechanism has been so difficult to understand is the inseparability of the different material changes caused by irradiation. The principal changes due to irradiation; microstructure (formation and growth of dislocation loops, voids, bubbles, phases), grain boundary chemistry (segregation of alloying and impurity elements to or from the grain boundary), and hardening, all follow a similar dose dependence [2]. At any irradiation dose, all three types of

* Corresponding author. Tel.: +1 734 764 5290; fax: +1 734 763 4540.
E-mail address: zjiao@umich.edu (Z. Jiao).

0022-3115/$ - see front matter © 2006 Elsevier B.V. All rights reserved.
doi:10.1016/j.jnucmat.2006.12.012

radiation effects are proceeding together at roughly the same rate, and it is difficult to ascribe the resulting cracking behavior to one or any combination of them. Hence, identification of the primary factors contributing to IASCC is a challenge.

In searching for these primary factors, a systemic study of 14 austenitic alloys was carried out by Busby et al. [3] in simulated light water reactor (LWR) water. By isolating most of the metallurgical variables (microchemistry, microstructure, hardening, etc.) that control IASCC susceptibility of austenitic alloys, they tried to identify the ones with the strongest impact on IASCC. Their study suggests that neither RIS, nor irradiation microstructure, nor hardening alone controls IASCC. However, the potential exists for a correlation between localized deformation and IASCC, where deformation is controlled through stacking fault energy (SFE) or the irradiated microstructure.

Early work showed that SFE may be linked to stress corrosion cracking [4,5]. It has been hypothesized recently [6] that low SFE and irradiation can promote localized deformation by enhancing planar slip. Planar slip results in greater transmission of strain to the grain boundary, which may help rupture the oxide film and initiate a crack at the grain boundary. Furthermore, more dislocations are fed to a grain boundary crack tip through planar slip, which could result in crack extension and a higher crack growth rate.

Although many papers have been published on the deformation microstructure of neutron-irradiated stainless steels, very few deal with proton-irradiated samples. A fair comparison of the deformation microstructures between these two types of irradiations is not available. However, the overall microchemistry, microstructure, hardening and SCC behavior of proton- and neutron-irradiated 304SS and 316SS samples were found to be in excellent agreement [7]. The deformation mode and deformation microstructures are similar in both proton- and neutron-irradiated stainless steels. For example, twinning is the main deformation mode for 316SS at room temperature for both proton- and neutron irradiations [8,9].

As the deformation in an irradiated alloy is mainly localized in the dislocation channels, it is important to characterize the amount of strain accumulated in these channels. This work was done in a previous study [10] and the results showed that at low applied strain, the average strain in the channel is higher in the low SFE alloys than that in the high SFE alloy. The result correlates well with the cracking behavior of these alloys tested in simulated BWR normal water chemistry conditions. However, the deformation microstructure of these alloys may provide an understanding of how these channels can contribute to IGSCC. Therefore, the objective of this study was to understand the potential impact of stacking fault energy (SFE) and irradiation on IASCC susceptibility by examining the deformation microstructure of proton-irradiated alloys.

2. Experimental

2.1. Alloy selection and sample preparation

Three austenitic alloys were selected for this study: alloy E (base 304), alloy H (304 + Si) and alloy L (304 + Cr + Ni). The compositions of these alloys are listed in Table 1 together with their SFEs predicted by Pickering's equation [11]. Among these three alloys, Alloy L has the highest SFE because of its high nickel content and alloy H has the lowest SFE due to the addition of silicon. Generally, the addition of nickel will increase the SFE in an iron-base stainless alloy while the addition of silicon, even small increases within the acceptable limits for stainless steels will significantly decrease SFE.

Alloys were used in the solution-annealed condition without any additional processing or preparation other than surface polishing and cleaning. After the tensile specimens (dimensions are shown in Fig. 1) were made, the surfaces were ground using SiC paper to a final finish of #4000 grit. The samples were then electropolished in a 60% phosphoric,

Table 1
Compositions (wt%) and calculated stacking fault energies of selected alloys

Alloy	Cr	Ni	Fe	Mn	Mo	Si	P	C	S	N	SFE (mJ/m^2)
H	18.2	12.4	67.3	1.0	0.02	1.05	<0.01	0.020	0.002	0.0005	27.5
E	18.8	12.4	67.8	0.9	0.04	0.04	<0.01	0.021	0.003	0.0003	40.5
L	25.2	25.1	48.6	1.0	0.02	0.03	<0.01	0.020	0.002	0.0005	59.7

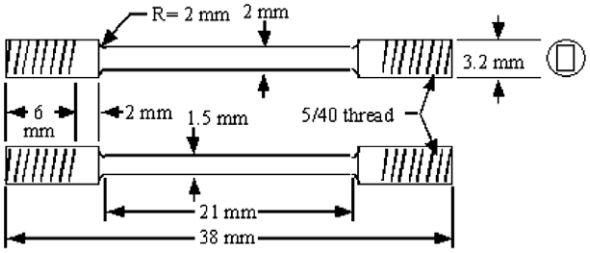

Fig. 1. Dimensions of the tested specimens.

40% sulfuric acid solution at room temperature to get a mirror like surfaces prior to irradiation experiment.

2.2. Proton irradiations and constant extension rate tensile (CERT) tests

Irradiations of sample were performed using a specially designed stage connected to the General Ionex Tandetron accelerator at the Michigan Ion Beam Laboratory. Irradiations were conducted using 3.2 MeV protons at a dose rate of approximately 8.5×10^{-6} dpa/s (the experimental doses and dose rates are calculated using SRIM2003 [12]), resulting in a nearly uniform damage rate through the first 35 μm of the proton range (total = ~40 μm). Irradiations were conducted to 1.0 and 5.5 dpa, where dpa is calculated using SRIM2003 with a displacement energy of 40 eV [13]. The sample temperature was maintained at 360 ± 10 °C for the duration of the irradiation.

The CERT tests were conducted in a multiple-specimen test system, supplied by KorrosData. The CERT setup consists of an autoclave, a load frame, and a computer driven, 30 kN load train for straining of the samples. Four independent tensile load cells measured the tensile force on each sample. After the tensile specimens were loaded, the autoclave was sealed and purged with flowing Ar to ensure that all air was removed from the autoclave. The system was then heated to 288 °C. After the temperature was stabilized, the load was applied and the specimens were pulled with a strain rate of 3.5×10^{-7}/s. The tests were interrupted at 3%, 7% and 12% applied strain for dislocation channel characterization.

2.3. Specimen examination methods

In this experiment, both the irradiation and the deformation microstructure were examined using a JOEL 2010F analytical transmission electron microscopy (TEM) at the University of Michigan Electron Microbeam Analysis Laboratory (EMAL). TEM specimens were made from the as-irradiated or strained samples by first grinding off the excessive material from the unirradiated side. Then 3 mm disks were cut using an ultrasonic slurry cutter. The disks were mechanically thinned to ~100 μm and then jet-thinned until perforation in a 5% perchloric acid and 85% methanol solution at −40 °C. The dislocation loops were examined using rel-rod dark field technique. The voids were imaged at slightly under-focus condition. Two-beam condition was used to examine dislocation channels and other features. The observations of the interactions between slip lines and grain boundaries on the surface of the strained samples were performed on a Philips 30XL FEG scanning electron microscopy (SEM) at EMAL.

3. Results and discussion

3.1. Proton-irradiation microstructure

Proton-irradiated austenitic alloys H, E and L have similar dislocation loop microstructure. The irradiation microstructure of alloys H, E and L irradiated to 1.0 dpa (Fig. 2 top) consists of high density of defect clusters and small loops (1–2 nm). As the dose increases to 5.5 dpa, faulted loops become the major feature (Fig. 2 bottom). The average loop sizes are comparable and around 10 nm for all alloys. The loop density is the lowest in alloy H (1.4×10^{22} m^{-3}) and the highest in alloy L (1.9×10^{22} m^{-3}). The higher loop density in alloy L may be due to its high Ni content. In a study of the influence of bulk Ni content on dislocation microstructure, Muroga et al. [14], reported a positive correlation between Ni content and dislocation loop density. The loop density increases with the Ni content in an Fe–15Cr–xNi series when the Ni content is less than 30 wt%.

Voids were found in alloy L at both doses and in alloy E only at 5.5 dpa (Fig. 3). No voids were observed in alloy H regardless of doses. Silicon is known to be an effective swelling inhibitor in neutron-irradiated 316 stainless steels in the wt% range of ~0.16–0.9 [15,16]. Similar influence of silicon content on void swelling was also found in proton-irradiated alloys [17]. Therefore, the addition of ~1% Si in alloy H is believed to suppress void swelling by increasing the vacancy diffusivity and

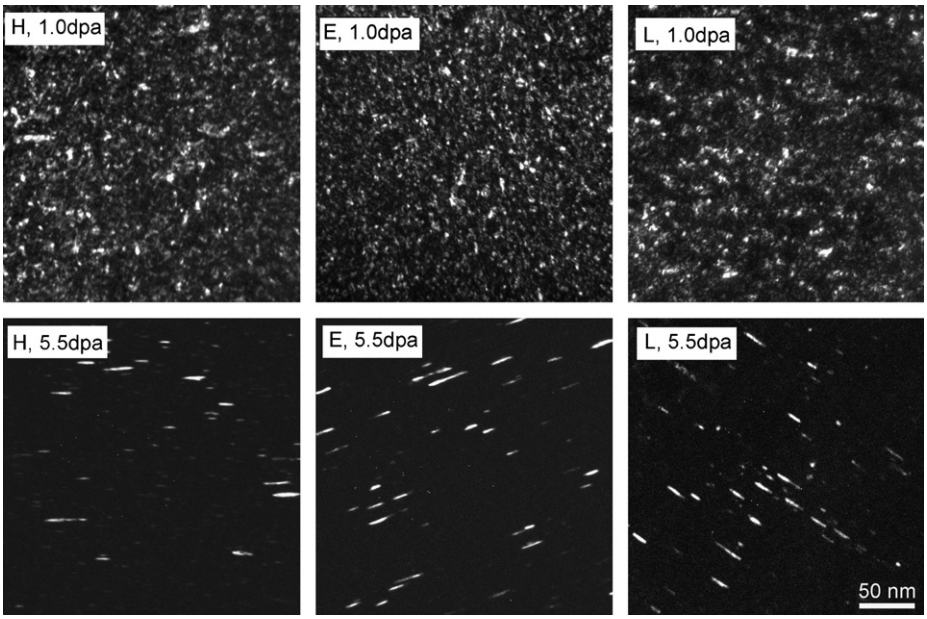

Fig. 2. TEM weak beam (top) and rel-rod (bottom) dark field images of defect clusters or dislocation loops in alloys H, E and L irradiated to 1.0 and 5.5 dpa. Images were taken near [1 1 0] beam direction.

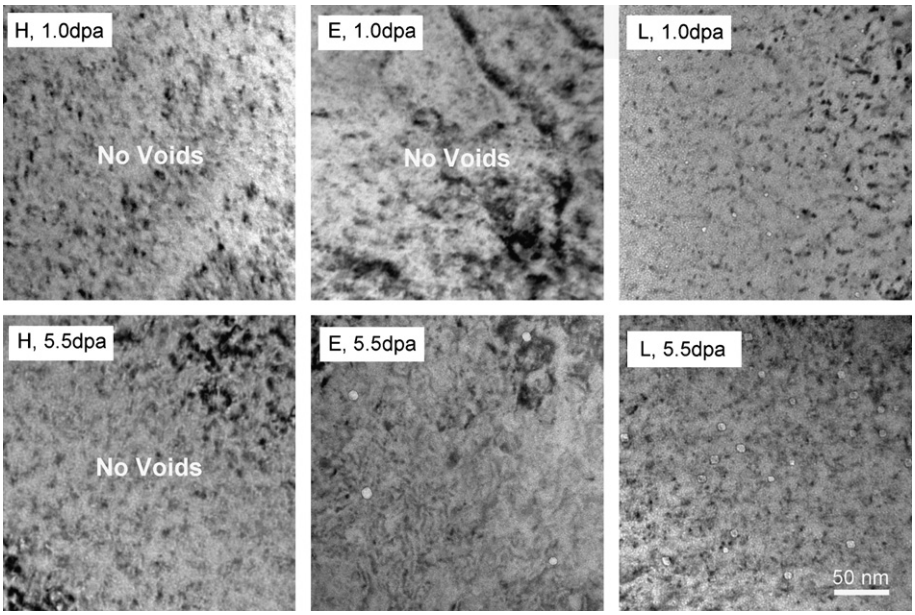

Fig. 3. Bright field TEM image of voids in alloys H, E and L irradiated to 1.0 and 5.5 dpa.

reducing the vacancy supersaturation [18]. The different void swelling behavior of alloys E and L at 1.0 dpa may be due to the difference in Cr and Ni content, as the swelling generally increases with increasing Cr and decreasing Ni [17,19].

Radiation-induced segregation (RIS) at grain boundaries for the three principal alloying elements of Cr, Ni and Fe was measured via STEM/EDS using the Philips CM200/FEG TEM-STEM at the Oak Ridge National Laboratory in alloys H, E and L proton-irradiated to 5.5 dpa at 360 °C. The CM200/FEG operates with an accelerating voltage of 200 kV and an incident beam size <1.4 nm. The wt% deviation in grain boundary composition from

bulk composition is shown in Fig. 4. For all alloys, Cr is depleted at grain boundaries. Alloy L has the largest degree of Cr depletion, while Alloy E has the lowest. The grain boundary Ni content was enriched above bulk levels for all alloys, with alloy E having the least Ni enrichment and alloy L the most. The grain boundary Fe content is at or near the bulk content for alloy E while alloy H and L have significant Fe depletion. Although a number of studies [20–22] have reported a link between intergranular stress corrosion cracking (IGSCC) and Cr depletion, this correlation is not shown in this study. For example, alloy L has the largest degree of Cr depletion, however, it is resistant to cracking in BWR normal water chemistry conditions. A lack of correlation between Cr depletion and IGSCC susceptibility was also observed by others. For instance, Jacobs et al. [23] identified significant Cr depletion (as low as 13.5 wt%) in a number of 316 SS alloys that were also resistant to cracking. Annealing studies of Busby et al. [24] showed that cracking was mitigated following post-irradiation annealing, while Cr depletion remained at the as-irradiated level.

The average composition for Fe, Cr and Ni at grain boundary for alloys H, E and L are shown in Fig. 5. The alloy L has higher Cr level (18 wt%) and alloys E and H have lower Cr level (16 and 13 wt%, respectively). Previous simulated BWR tests [10] showed that both alloys E and H exhibited IG cracking and the percentages are 38.7% and 58.6%, respectively. No IG cracking was found in alloy L. The total crack length was 40.5 mm for alloy H and 9.2 mm for alloy E. Although the grain boundary Cr correlates with the degree of cracking, the differences are small and are unlikely to explain the large differences in observed degree of IGSCC.

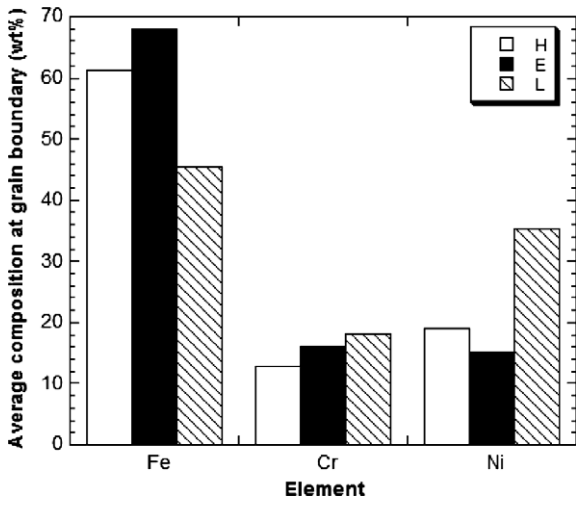

Fig. 4. Average composition at grain boundary for alloys H, E and L proton-irradiated to 5.5 dpa at 360 °C.

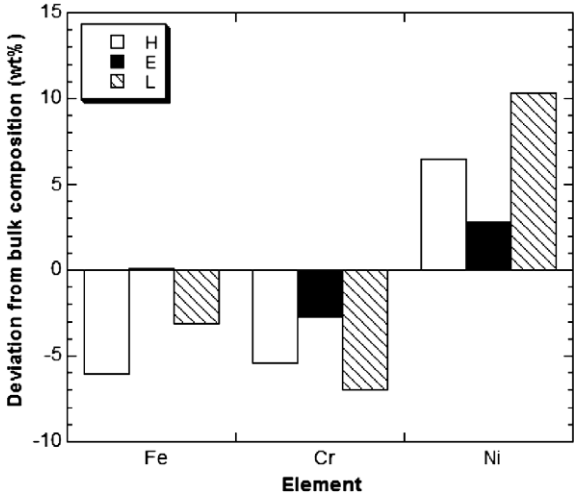

Fig. 5. Change in grain boundary composition from bulk composition for alloys H, E and L proton-irradiated to 5.5 dpa at 360 °C.

3.2. SEM observations of interactions between slip lines and grain boundaries

SEM observations of the strained samples show three types of interactions between slip lines and grain boundaries. Slip transmission from one grain to an adjoining grain (Fig. 6(a)) was commonly found in all three alloys, especially at higher strain levels. At low strain, slip lines tended to terminate at grain boundaries (Fig. 6(b)). Grain boundary sliding was found in alloy L irradiated to 1.0 dpa and strained to 12% (Fig. 6(c)). Deformation ledges (Fig. 6(d)) were formed in alloy E irradiated to 5.5 dpa and strained to 7%.

As mentioned by Was et al. [6], the transmission of slip from one grain to an adjacent grain will relieve the stress at the grain boundary. The magnitude of the stress relief is dependent on how well the slip systems in adjoining grains match. Since the most likely slip system to be activated is the one with the maximum resolved shear stress and the minimum angle between the slip planes [25], the amount of stress relieved by transmission is generally large and the deformation at the grain boundary caused by slip transmission is small. Therefore, the propensity for stress corrosion cracking at these

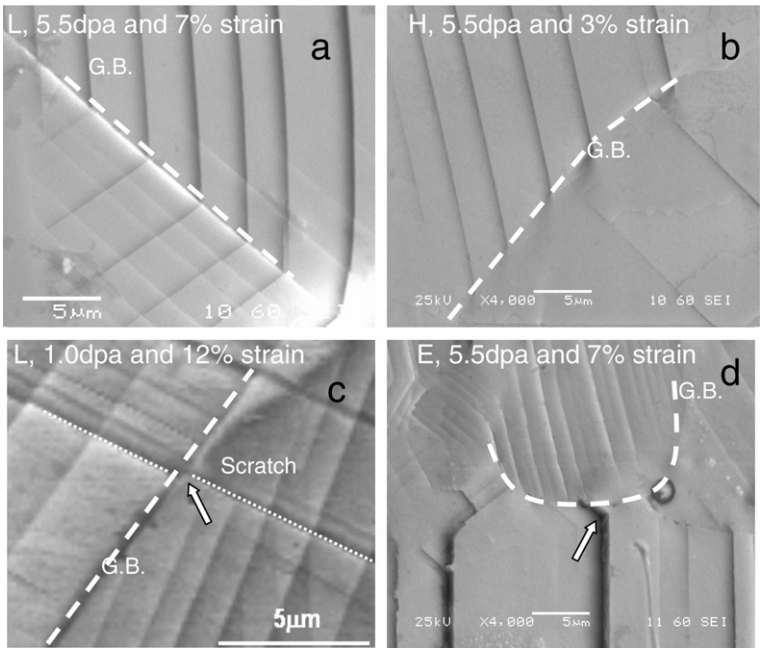

Fig. 6. Types of interactions between dislocation channels and grain boundaries: (a) slip transmission from one grain to another, (b) slip termination at grain boundary, (c) grain boundary sliding and (d) deformation ledge formation at grain boundary. Arrows indicate an offset on a scratch (dotted line) caused by grain boundary sliding in (c) and a deformation ledge at grain boundary in (d).

boundaries is low. If the slip lines terminate at a grain boundary, the stress or strain could be low or high depending on how many dislocations are piled-up at the grain boundary. If the deformation at the grain boundary is large, grain boundary sliding and deformation ledge may be observed. Grain boundary sliding can rupture the oxide film at grain boundary and therefore, increase the IGSCC susceptibility. Deformation ledges are associated with a large strain field and may facilitate the initiation of microcracks.

3.3. Deformation microstructure – TEM observations

TEM experiments were performed on alloys H, E and L at 1.0 dpa and 12% strain and 5.5 dpa and 7% strain. At 1.0 dpa, planar slip of dislocations was observed in alloy H and E as indicated by arrows in Fig. 7(a) and (b). Wavy slip was found in alloy L (Fig. 7(d)). A higher magnification image (Fig. 7(c)) shows that the dislocation band consists of dislocations and defect clusters. The slip in alloys H, E and L is likely controlled by the SFE other than the irradiation at 1.0 dpa. It is known that stacking fault energy can strongly influence the deformation mode by affecting the dislocation slip and cross-slip behavior. High stacking fault energy promotes cross-slip while low stacking fault energy results in widely spaced partial dislocations that impede dislocation cross-slip. Therefore, the high SFE in alloy L facilitates cross-slip while the low SFE in alloys H and L promotes planar slip, consistent with these results.

At 5.5 dpa, dislocation channeling becomes the major deformation mode for all three alloys (Fig. 8(a)) as the irradiated microstructure dominates the SFE effect. High magnification image shows that the dislocation channels are nearly defect-free (Fig. 8(b)). No dislocations were observed in between dislocation channels, which implies that dislocations mainly glide in channels. As a result, higher channel strain and slip planarity are expected in samples at 5.5 dpa.

Deformation twins were observed in low stacking fault energy alloys H and E (Fig. 8(c)). The critical stress for twinning under a uniaxial stress can be given as [26]:

$$\sigma_T = \frac{\gamma_{SF}}{b},$$

where γ_{SF} is the stacking fault energy and b is the magnitude of the Burgers vector. This equation shows that stress for twinning is heavily dependent on SFE. Lower stress is needed for twinning in

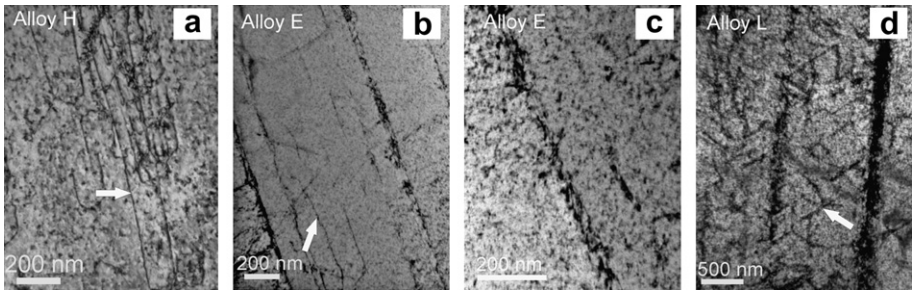

Fig. 7. Deformation microstructure in alloys H, E and L irradiated to 1.0 dpa and strained to 12%.

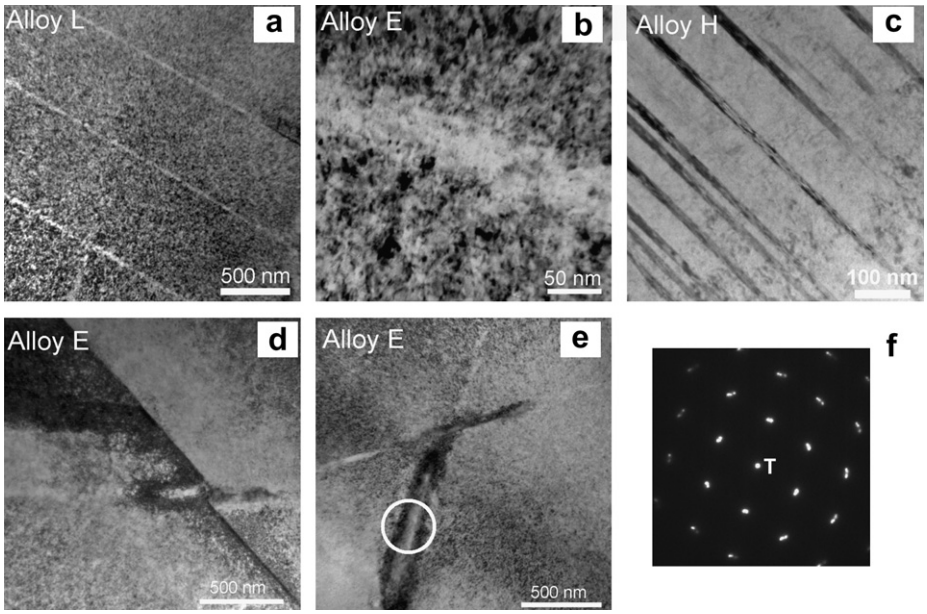

Fig. 8. Deformation microstructure in alloys H, E and L irradiated to 5.5 dpa and strained to 7%: (a) dislocation channels, (b) a dislocation channel at high magnification, (c) deformation twins, (d) an expanded channel intersecting a grain boundary, (e) channel expansion at a channel–channel intersection, and (f) selected area diffraction pattern taken from the expanded channel in (e) showing atomic planes rotation.

lower SFE alloys. Twins with high planarity have similar behavior to defect-free dislocation channels when they are intersecting grain boundaries.

Channel expansion was a commonly observed feature in alloys H and E at locations where dislocation channels intersect grain boundaries (Fig. 8(d)) or other channels (Fig. 8(e)). The expanded regions are generally several times as wide as other locations in a dislocation channel and several hundred nanometers to more than 1 μm long. When the expanded channel intersects a grain boundary, a step is formed at the grain boundary as shown in Fig. 8(d). A selected area diffraction (SAD) pattern (Fig. 8(f)) from the expanded channel shows that it is neither a twin nor martensite. It is just a systemic rotation of atomic planes in the expanded channel relative to those in adjacent area. Channel expansion was also observed in the high SFE alloy L, but at a much reduced frequency.

Fig. 9(a) shows another example of expanded channels intersecting a grain boundary in alloy E at 5.5 dpa and 7% strain. A step is formed at the grain boundary when the lower expanded channel intersects the grain boundary. SAD of the upper expanded channel shows a $\sim 3^\circ$ rotation of the atomic planes around the [0 1 1] zone axis in the expanded channel relative to the matrix. The rotation corresponds to a 5% shear strain and is applied to the grain boundary. Therefore, as illustrated in Fig. 10, when an expanded channel intersects a

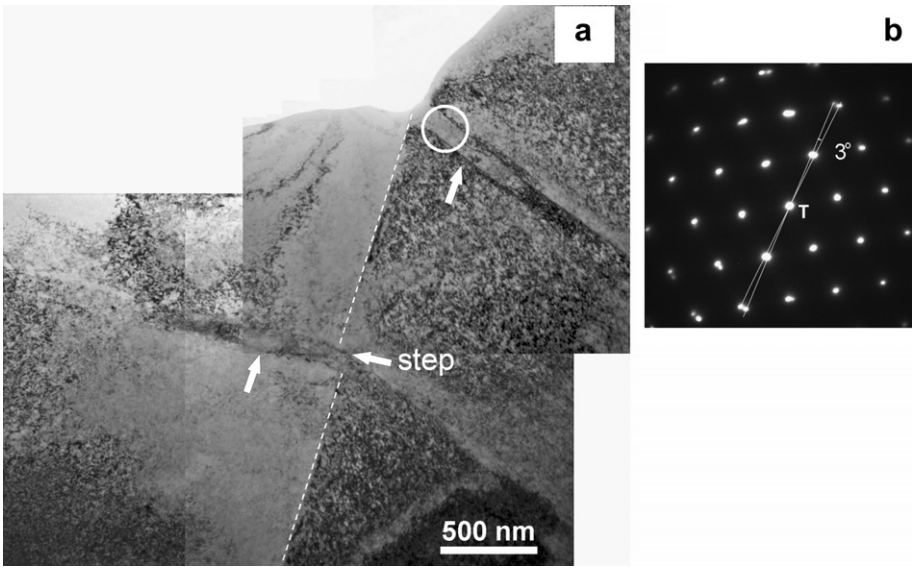

Fig. 9. (a) Bright field TEM image of two expanded channels intersecting a grain boundary in alloy E irradiated to 5.5 dpa and strained to 7%, (b) selected area diffraction pattern from the upper expanded channel. Arrows indicate the expanded channels and a step at grain boundary. Dashed line indicates the position of the grain boundary.

grain boundary, not only it forms a step, but also it generates shear strain at the grain boundary. This additional shear strain, when combined with a step at grain boundary, may play an important role in IGSCC. Thomas et al. [27] reported that cracks in the cold-worked Type 316SS PWR baffle bolt narrowed in a series of discrete steps that occurred at shear band intersections. Furthermore, the crack advance appeared to be discontinuous and related to some deformation events in the matrix. However, no stepped structures were observed at the crack walls in the unirradiated stainless steel service components exposed to high-temperature water environments. The discrepancy in crack morphologies may be due to the different deformation microstructure in irradiated and unirradiated stainless steels. Cracks in the irradiated stainless steel are likely to initiate at steps that are formed at the grain boundary because of the stress/strain concentration at these locations. Once a crack initiates, it can propagate along the grain boundary until it meets another step. Because of the grain boundary misalignment as a result of the steps, the crack tip will rest at the step. When the stress at the step is high enough to overcome the obstacle due to the misalignment, the crack will advance. However, in the unirradiated steels, fine slip lines are relatively uniformly distributed. Steps caused by slip lines are generally insignificant.

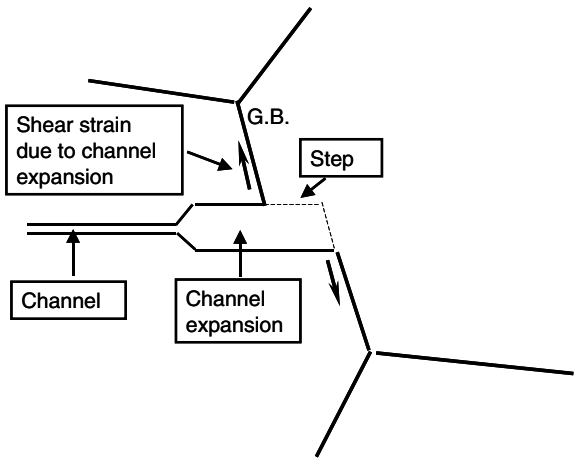

Fig. 10. Schematic showing an expanded channel intersecting a grain boundary.

Steps were observed on grain boundary fracture surfaces in both neutron-irradiated 304 stainless steel [28] and in proton-irradiated alloys strained under LWR conditions (steps are indicated by arrows in Fig. 11) [29]. They were also observed on the IG fracture surface of neutron-irradiated thermally sensitized 304 SS strained in inert gas [30]. All these observations provide additional evidence that the IGSCC may be related to the localized deformation in steps or dislocation channels.

In the present study, steps associated with channel expansion were found predominately in low SFE

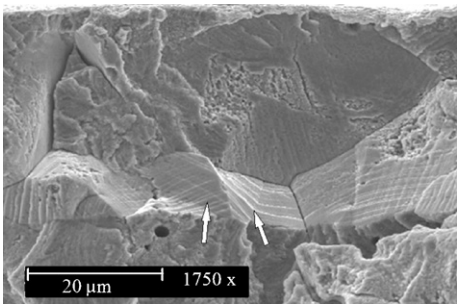

Fig. 11. Fracture surface of 304 SS irradiated with protons at 360 °C and strained to failure in simulated BWR environment [29]. Steps are indicated by arrows.

alloys H and E at 5.5 dpa. However, the density of expanded channels in high SFE alloy L was much reduced. In other words, a higher degree of localized deformation due to steps and dislocation channels were found in low SFE alloys. This is consistent with the cracking behavior of alloys H, E and L irradiated to 5.5 dpa and tested in BWR under normal water chemistry conditions, in which alloys H and E are susceptible to IGSCC while alloy L is resistant to cracking. Furthermore, steps were only observed in alloy at high dose. There were no steps observed in any of the three alloys at 1.0 dpa. Irradiation dose, therefore, plays a role in IGSCC by increasing the degree of localized deformation in steps and dislocation channels.

4. Conclusions

Proton-irradiated austenitic alloys H, E and L have similar dislocation loop microstructure. At 1.0 dpa, the irradiation microstructure mainly consists of high density of defect clusters and small dislocation loops. Large faulted loops (~10 nm) were found in these alloys at 5.5 dpa. Voids were found in alloy L at 1.0 and 5.5 dpa and in alloy E at 5.5 dpa. No voids were observed in alloy H regardless of dose. RIS measurements showed that Cr was depleted while Ni was enriched at grain boundaries. The depletion of Cr at grain boundaries does not fully explain the observed large difference in IGSCC behavior among studied alloys.

Three types of interactions between slip lines and grain boundaries were identified. They were slip transmission from one grain to another, grain boundary sliding and ledge formation at grain boundaries. Grain boundary sliding and deformation ledges result in great deformation at grain boundaries.

Dislocation bands in alloys H, E and L irradiated to 1.0 dpa and strained to 12% consist of dislocations and defect clusters. Planar slip is found in alloys H and E while wavy slip is found in alloy L. The different morphologies of dislocation slip may be due to the difference in SFEs.

Near defect-free dislocation channels were observed in alloy H, E and L irradiated to 5.5 dpa and strained to 7%. Channel expansion was found predominantly in alloys H and E at locations where channels intersecting with grain boundaries or other channels. Fewer expanded channels were found in alloy L. Channel expansion results in steps and additional strain at grain boundaries. The localized deformation in steps and dislocation channels may be related to the IASCC susceptibility.

Acknowledgements

The authors gratefully acknowledge Victor Rotberg and Ovidiu Toader for their assistance in conducting proton irradiations. The authors also acknowledge the facilities provided by the Michigan Ion Beam Laboratory and the Electron Microbeam Analysis Laboratory at University of Michigan. Support for this research was provided by the department of energy (DOE) and the Cooperative IASCC Research (CIR) program.

References

[1] P.L. Andresen, F.P. Ford, S.M. Murphy, J.M. Perks, in: Proceedings of 4th International Symposium on Environmental Degradation of Materials in Nuclear Power Systems – Water Reactors, NACE International, Houston, 1990.
[2] G.S. Was, in: Proceedings of 11th International Symposium on Environmental Degradation of Materials in Nuclear Power Systems – Water Reactors, American Nuclear Society, La Grange, IL, 2003, p. 965.
[3] J.T. Busby, G.S. Was, in: Proceedings of 11th International Conference on Environmental Degradation of Materials in Nuclear Power Systems – Water Reactors, American Nuclear Society, La Grange Park, IL, 2004, p. 995.
[4] P.R. Swann, Corrosion 19 (1963) 102.
[5] A.W. Thompson, I.M. Bernstein, in: R.W. Staehle, M.G. Fontana (Eds.), Advances in Corrosion Science and Technology, 7, Plenum, New York, 1980, p. 53.
[6] G.S. Was, B. Alexandreanu, J. Busby, Advances in Fracture and Failure Prevention, Trans Tech, Switzerland, 2004, p. 885.
[7] G.S. Was, J.T. Busby, T. Allen, E.A. Kenik, A. Jenssen, S.M. Bruemmer, J. Gan, A.D. Edwards, P.M. Scottf, P.L. Andresen, J. Nucl. Mater. 300 (2002) 198.
[8] K. Farrell, T.S. Byun, N. Hashimoto, J. Nucl. Mater. 335 (2004) 471.

[9] C. Bailat, F. Gröschela, M. Victoria, J. Nucl. Mater. 276 (2000) 283.
[10] Z. Jiao, J.T. Busby, R. Obata, G.S. Was, in: Proceedings of 12th International Conference on Degradation of Materials in Nuclear Power Systems – Water Reactors, The Minerals, Metals and Materials Society, Warrendale, PA, 2005, p. 379.
[11] F.B. Pickering, in: Proceedings of Conference on Stainless Steels 84, Gothenberg, Sweden, 1984, The Institute of Metals, London, 1985, p. 2.
[12] J.F. Ziegler, J.P. Biersack, SRIM2003 program, IBM Corp., Yorktown, NY.
[13] ASTM Designation E 521-89, Annual Book of ASTM Standards, Vol. 12.02, American Society for Testing and Materials, Philadelphia, PA, 1989, p. D-9.
[14] T. Muroga et al., ASTM STP 1125, 1992, p. 1015.
[15] J.F. Bates, J.J. Holmes, M.M. Paxton, J.L Straaslund, US Patent. 3856517, 1974.
[16] H.R. Brager, ASTM STP 570, 1975.
[17] G.S. Was et al., J. Nucl. Mater. 270 (1999) 96.
[18] F.A. Garner, W.G. Wolfer, J. Nucl. Mater. 102 (1981) 143.
[19] J.F. Bates, W.G. Johnston, in: Proceedings of International Conference on Radiation Effects in Breeder Reactor Structural Materials, Scottsdale, The Metallurgical Society of AIME, New York, 1977, p. 625.
[20] S.M. Bruemmer, Mater. Sci. Forum 46 (1989) 309.
[21] S.M. Bruemmer, L.A. Charlot, Scr. Metall. 20 (1986) 1010.
[22] P.L. Andresen, in: D. Cubicciotti (Ed.), Proceedings of Fifth International Symposium on Environmental Degradation of Materials in Nuclear Power Systems – Water Reactors, ANS, Monterey CA, 1992, p. 209.
[23] A.J. Jacobs, G.P. Wozadlo, K. Nakata, S. Kasahara, T. Okada, S. Kawano, S. Suzuki, Proceedings of Sixth International Symposium on Environmental Degradation of Materials in Nuclear Power Systems – Water Reactors, R.E. Gold, E.P. Simonen (Eds.), TMS, 1993, p. 597.
[24] J.T. Busby, G.S. Was, E.A. Kenik, J. Nucl. Mater. 302 (2002) 20.
[25] W.A.T. Clark, R.H. Wagoner, Z.Y. Shen, T.C. Lee, I.M. Robertson, H.K. Birnbaum, Scr. Metall. Mater. 26 (1992) 203.
[26] T.S. Byun, Acta Mater. 51 (2003) 3063.
[27] L.E. Thomas and S.M. Bruemmer, Proceedings of 11th International Conference on Environmental Degradation of Materials in Nuclear Systems, Stevenson, WA, August 10–14, 2003. p. 1049.
[28] R.E. Clausing, E.E. Bloom, in: J.L. Walter, J.H. Westbrook, D.A. Woodford (Eds.), Claitors, Baton Rouge, LA, 1975.
[29] J.T. Busby, PhD Thesis, University of Michigan, 2001.
[30] T. Onchi et al., J. Nucl. Mater. 340 (2005) 219.